3D High-Resolution Modeling of Aircraft-Induced NO$_x$ Emission Dispersion in CAEPport Configuration Using Landing and Take-Off Trajectory Tracking

W. Ghedhaïfi · E. Montreuil · M. Chouak · F. Garnier

Abstract Pollutant emissions from aircraft operations contribute to the degradation of air quality in and around airports. Meeting the ICAO's environmental certification standards regarding both gaseous and particulate aircraft engine emissions is one of the main challenges for air-transportation development over the coming years. To increase the accuracy of airport air pollution monitoring and prediction, advanced decision-making tools need to be developed. In this context, the present study aimed at demonstrating the modeling capabilities of an innovative methodology that accounts for the microscale evolution of aircraft emissions, both spatially and temporally. For this purpose, 3D high-resolution CFD simulations were carried out in the CAEPport configuration (medium-size mock airport) as defined by the Committee on Aviation Environmental Protection (CAEP/8) for local air-quality assessment. The modeled domain extends up to 8 km around the airport. A spatial resolution down to 1 m was used around buildings to refine the prediction of pollutant-emission concentrations. The model accounts for ambient meteorological conditions along with the background chemical composition. NO$_x$ emissions from main engines and auxiliary power units (APUs) were individually tracked along LTO trajectories with a time resolution down to 1 s. The impact of atmospheric stability was investigated in three cases, i.e., stable, neutral, and unstable. The results show NO$_2$ dominating in apron areas due to the low power setting of main engines along APU contribution during extended parking. Conversely, a domination of NO emissions was observed at the runway threshold due to the high power setting of the main engines. Stable atmospheric conditions promoted higher NO and NO$_2$ concentrations as compared to both neutral and unstable cases. The use of APUs contributed to higher concentrations of both NO and NO$_2$ emissions and especially of NO$_2$ in terminal areas.

Nomenclature

LTO	Landing and take-off
CAEP	Committee on aviation environmental protection
ICAO	International civil aviation organization
MDG	Modeling and Databases Group
LAQ	Local air quality
APU	Auxiliary power unit

W. Ghedhaïfi · E. Montreuil
Multi-Physics Department for Energetics, ONERA, University of Paris Saclay, 91123 Palaiseau, France

M. Chouak (✉) · F. Garnier
Department of Mechanical Engineering, ÉTS, University of Quebec, Montreal, QC, Canada
e-mail: mohamed.chouak.1@ens.etsmtl.ca

ARP	Airport reference point
UFP	Ultra-fine particle
vPM	Volatile particle matter
nvPM	Non-volatile particle matter
Symbols L_x, L_y, L_z	Length of the computational domain in x-, y-, and z-directions, in m
$\bar{\rho}$	Mean density of the gas mixture, in kg/m³
$\bar{p}$	Mean pressure of the gas mixture, in Pa
$\bar{p}_t$	Mean total pressure of the gas mixture, in Pa
$\bar{T}$	Mean static temperature of the gas mixture, in K
$\bar{T}_t$	Mean total temperature of the gas mixture, in K
RH	Relative humidity, in %
$\bar{N}_s$	Mean concentration of soot particles, in #/cm³
$\tilde{u}_i$	Favre average velocity, ith component, in m/s
$\tilde{y}_k$	Favre average mass fraction of kth specie, in kg/kg
D_k	Diffusion coefficient for the kth specie, in m²/s
c_p	Specific heat capacity at constant pressure for the gas mixture, in J/kg
g	Gravitational acceleration on the earth's surface
μ	Dynamical viscosity of the gas mixture, in kg/(m.s)
$\tilde{e}$	Favre average internal energy of the gas mixture, in J/kg
$\tilde{e}_t$	Favre average total energy of the gas mixture, in J/kg
$\tilde{h}_t$	Favre average total enthalpy of the gas mixture, in J/kg
$\tilde{S}_{ij}^d$	Deviator strain-rate tensor, in s⁻¹
$\widetilde{u_i^\varepsilon u_j^\varepsilon}$	Reynolds stress tensor, in m²/s²
$\widetilde{u_j^\varepsilon T^\varepsilon}$	Turbulent heat vector, in K.m/s
$\widetilde{u_j^\varepsilon y_k^\varepsilon}$	Turbulent mass flux vector, in kg.m/(kg.s)

1 Introduction

The air quality in airports is becoming an important issue that has to be addressed as air traffic will keep growing by + 3.6% annually between 2018 and 2050 according to the latest ICAO's long-term traffic forecasts (ICAO, 2021). Even though the pandemic has had an undeniable impact on air-transportation development at least in the short term (Nižetić, 2020) (the passenger air traffic fall between 2019 and 2020 was about 60%), a world recovery to pre-COVID-19 levels is estimated in late 2022 (Gudmundsson et al., 2021). As such, concerns related to air-traffic pollutant emissions (nitrogen oxides (NO_x), hydrocarbons (HC), carbon monoxide (CO), and particulate matter (PM)) require particular attention, especially in the vicinity of airports, by means of in situ monitoring and/or numerical investigations (Yim et al., 2015). Their impact on both human health and environment makes the surveillance and the search for mitigation strategies essential. In this context, the study of air quality in and around airports has attracted growing interest both experimentally and numerically.

Several studies have investigated the impact of airport emissions on local air quality as performed in Munich (Suppan & Graf, 2000), Frankfurt (Crecelius & Sommerfeld, 2005), and Heathrow (Farias & ApSimon, 2006). The study of airport emission dispersion involves different sources, such as aircraft landing and takeoff (LTO) operations, airport infrastructure operations, and road traffic from/to the airport. The complete listing of airport emissions by groupings can be found in Chester and Horvath (2009). This paper focuses on the dispersion of air-traffic emissions. LTO operations include various emission sources such as the main aircraft engines and ground handling operations (cabin service, catering, luggage/cargo handling, ground power, etc.). The latter includes fuel-powered tugs and ground carts, known as ground-support equipment (GSE), as well as auxiliary power units (APUs), either installed on equipped aircrafts or in-ground carts for non-equipped aircrafts (Kinsey et al., 2012). APUs provide a source of electrical power and compressed air to operate onboard avionic and air-conditioning (A/C) systems and for main-engine start.

For a long time, aircraft emissions during LTO operations were conventionally considered to account for most pollutant emissions in airports (Masiol & Harrison,

2014). Emission inventories performed at several international airports (Celikel et al., 2004; Mazaheri et al., 2011; Winther et al., 2015; Yang et al., 2018; Yim et al., 2013) have shown, however, that the impact of ground handling emissions was as high as that of LTO emissions. As such, airports are mainly concerned about NO_x emissions (especially NO_2 which is regulated). For example, the study of emissions at the Zurich airport (Celikel et al., 2004) indicates that the GSE-related NO_x emissions were of the same order as the LTO-related emissions. For instance, the APU share of NO_x emissions was as high as 40–50% of total GSE emissions. The emission inventory performed at the Copenhagen airport (Winther et al., 2015) show that, in addition to gaseous pollutants, APUs were the largest contributor of PM (particulate matter) in the inner apron area in number (54%) as compared to main engine (43%) and handling (2.4%) contributions. Black carbon (BC) measurements in 12 airports (Targino et al., 2017) also confirmed that the most polluted airport areas were found in concourse (including all indoor areas in the airport terminal, such as check-in counters and gatehouses) and transit areas between the aircraft and concourse (by apron bus, jet bridge, or pedestrian walkway). These findings highlight the importance of investigating the impact of both LTO and APU emissions on airport air quality.

The study of airport air quality using numerical tools has received more interest in the last few decades as compared to field measurements, since it yields a better understanding of the impact of a specific source in a realistic airport configuration. Modeling airport air quality is particularly complex since it involves multi-scale phenomena such as microscale dispersion, volatile and non-volatile PM microphysics, and gaseous chemistry of fuel combustion products. Four main approaches are proposed in the literature for dispersion modeling, namely Gaussian, Lagrangian, Eulerian, and hybrid.

The Gaussian models, also known as fast-response models, use a simple analytical equation (Gaussian distribution) to compute pollutant concentrations. The low computational cost associated with Gaussian models makes it possible to investigate the long-term impacts of aviation on air quality. To compensate for the shortcomings inherent in flow representation, they usually integrate complex dispersion processes (Tominaga & Stathopoulos, 2013); e.g., atmospheric stratification, buoyancy, chemistry, deposition, and concentration fluctuations. Gaussian models were used in airport

environments (Celikel et al., 2004; Henry-Lheureux et al., 2021; Mazaheri et al., 2011; Winther et al., 2015; Yang et al., 2018; Yim et al., 2013) to develop a comprehensive formal assessment of emission inventories (aircraft main engines, APUs, ground-support equipment (GSE), ground-access vehicles (GAVs), private vehicle, stationary sources, etc.), because they are designed to enable different sources of pollutants (Winther et al., 2015) (main engines, APUs, GSE, etc.). For example, a Gaussian model was used to study NO_x and CO emissions from Montreal's international airport (YUL) (Henry-Lheureux et al., 2021). The study investigated the impact of both air traffic and GAVs on the whole island of Montreal (56×40 km) discretized with a spatial resolution of 110 m. Results under different atmospheric conditions show that pollutants were dispersed further and their concentrations higher during the winter season than in the summer season. Low-resolution Gaussian modeling, however, does not allow for the accurate identification of persistent high-concentration spots (or hotspots) within the airport areas. For instance, Gaussian models are not designed to address low wind conditions within complex environments and explicit building obstacles (Sarrat et al., 2017; Tominaga & Stathopoulos, 2013). The spatial representation of pollutant concentration distributions remain limited as complex 3D flow patterns around airport buildings, like recirculation or horseshoe vortices, cannot be captured with Gaussian models (Tominaga & Stathopoulos, 2016).

Alternatively, computational fluid dynamics (CFD) or Eulerian high-resolution models can yield more detailed descriptions of local and short-term dynamics (Tominaga & Stathopoulos, 2016). Two CFD approaches have been considered in the literature for modeling pollutant dispersion: large eddy simulation (LES) and Reynolds-averaged Navier–Stokes (RANS) equations. The LES approach is known to be more accurate in predicting turbulent flow characteristics compared to the RANS approach. Given the relatively high computational costs associated with LES modeling (Zhang et al., 2020), its use in modeling pollutant dispersion has been restricted to isolated building studies (Du et al., 2020). In contrast, the RANS approach has been used for various pollutant dispersion applications, such as isolated buildings (Santos et al., 2009; Tominaga & Stathopoulos, 2009), urban areas (Hanna et al., 2006; Pontiggia et al., 2010), and street canyons (Mei et al., 2019). Despite the rich literature on pollutant dispersion modeling in urban environments, only a few RANS studies have been conducted

in airport environments. For instance, the feasibility of CFD dispersion modeling for studying airport air quality was demonstrated by Sarrat et al. (2017), who coupled real-day air traffic data with a mesoscale atmospheric model (Sarrat et al., 2017). This study put forth a promising approach for accurately locating hotspots on the airport scale.

In this context, advanced decision-making tools need to be developed to increase the accuracy of airport air pollution monitoring and prediction. As such, our work aimed at demonstrating the modeling capabilities of a more advanced methodology that accounts for the microscale evolution of aircraft emissions, both spatially and temporally, along with the background chemical composition. For this purpose, high spatiotemporal resolution simulations of NO_x emission dispersion were carried out with the ONERA CFD code, CEDRE (Refloch et al., 2011). The CAEPport configuration (medium-size mock airport) was used as defined by the Committee on Aviation Environmental Protection (CAEP/8) for local air-quality assessment (ICAO, 2015).

2 Model Description

2.1 Governing Equations

The numerical methods in the CFD CEDRE code used in our study are based on a cell-centered finite-volume approach for general unstructured grids. The numerical code is a 3D multispecies compressible Navier–Stokes solver (Refloch et al., 2011). The compressible Reynolds-averaged Navier–Stokes (RANS) equations solved read as follows (Einstein notation):

$$\frac{\partial(\overline{\rho}\widetilde{y}_k)}{\partial t} + \frac{\partial(\overline{\rho u_j}\widetilde{y}_k)}{\partial x_j} = \frac{\partial}{\partial x_j}\left(\overline{\rho}D_k\frac{\partial\widetilde{y}_k}{\partial x_j} - \overline{\rho u_j''y_k''}\right) \quad (1)$$

$$\frac{\partial(\overline{\rho}\widetilde{u}_i)}{\partial t} + \frac{\partial(\overline{\rho u_j}\widetilde{u}_i)}{\partial x_j} = -\frac{\partial\overline{p}}{\partial x_i} - \overline{\rho}g\delta_{i3} + \frac{\partial}{\partial x_j}\left(\mu\widetilde{S}_{ij}^d - \overline{\rho u_i''u_j''}\right) \quad (2)$$

$$\frac{\partial(\overline{\rho}\,\widetilde{e}_t)}{\partial t} + \frac{\partial(\overline{\rho\widetilde{u}_j}\widetilde{h}_t)}{\partial x_j} = \frac{\partial}{\partial x_j}\left(\begin{array}{c}\overline{\rho}\,c_p\alpha\frac{\partial\overline{T}}{\partial x_j} + \sum_k\overline{\rho}\,\widetilde{h}_k\,D_k\frac{\partial\widetilde{y}_k}{\partial x_j} - \sum_k\overline{\rho}\,\widetilde{h}_k\,\widetilde{u_j^\varepsilon y_k^\varepsilon} \\ -\overline{\rho}\,\widetilde{u_j^\varepsilon T^\varepsilon} + 2\mu\widetilde{S}_{ij}^d - \overline{\rho}\,\widetilde{u_i^\varepsilon u_j^\varepsilon}\,\widetilde{u}_i \end{array}\right) \quad (3)$$

Compressibility effects are accounted for in the latter equations, and a density-weighted decomposition, also called Favre decomposition, is expressed with the tilde

sign ($\widetilde{}$) was used. Each given flow variable Φ is decomposed into a Favre average $\widetilde{\Phi} = \overline{\rho\Phi}/\overline{\rho}$ and a fluctuation Φ', i.e., $\Phi = \widetilde{\Phi} + \Phi''$, such as the overline sign ($\overline{}$) indicates time averaging. The term u_i denotes the velocity components, p is the pressure, T temperature, and e_t total energy ($e_t = e + u_iu_i/2$, such as e is the internal energy); h_t total enthalpy ($h_t = e_t + P/\rho$), $\widetilde{S}_{ij}^d$ the traceless deviatoric strain-rate tensor ($\widetilde{S}_{ij}^d = (\partial u_i/\partial x_j + \partial u_j/\partial x_i) - {}^2/_3\,(\partial u_k/3\partial x_k)\delta_{ij})$, g the gravitational acceleration on earth's surface, and ρ and μ are the mixture density and dynamic viscosity, respectively. The species are governed by their mass fraction y_k and their diffusion coefficient in the mixture D_k. The thermal diffusivity is represented by α.

2.2 Turbulence Model

The Reynolds tensor ($\overline{\rho\widetilde{u_i^\varepsilon u_j^\varepsilon}}$) is given by a Boussinesq hypothesis, while the turbulent diffusion fluxes of species and heat (respectively, $\overline{\rho\widetilde{u_j^\varepsilon T^\varepsilon}}$ and $\overline{\rho\widetilde{u_j^\varepsilon y_k^\varepsilon}}$) were assessed in analogy with molecular diffusion flux as follows:

$$\overline{\rho\widetilde{u_i^\varepsilon u_j^\varepsilon}} = \mu_t\widetilde{S}_{ij}^d + {}^2/_3\,\overline{\rho}k\delta_{ij} \quad (4)$$

$$\overline{\rho\widetilde{u_j^\varepsilon T^\varepsilon}} = -\overline{\rho}\alpha_t\frac{\partial\overline{T}}{\partial x_j} = -\frac{\mu_t}{Pr_t}\frac{\partial\overline{T}}{\partial x_j} \quad (5)$$

$$\overline{\rho\widetilde{u_j^\varepsilon y_k^\varepsilon}} = -\overline{\rho}D_{k,t}\frac{\partial\widetilde{y}_k}{\partial x_j} = -\frac{\mu_t}{Sc_{k,t}}\frac{\partial\widetilde{y}_k}{\partial x_j} \quad (6)$$

where the terms μ_t, Pr_t, and $Sc_{k,t}$ correspond to the turbulent eddy viscosity, turbulent Prandtl number, and turbulent Schmidt number, respectively. For turbulence closure, the hybrid Menter *SST k-ω* model (Menter, 1994) was used because of its good performance in modeling pollutant dispersion within complex built environments as stated in (Yu & Thé, 2016). Hence, two additional transport equations are introduced, i.e., Eqs. (7) and (8) for turbulent kinetic energy k and turbulent dissipation rate ω, respectively. The eddy viscosity is derived from k and ω ($\mu_t = \rho k/\omega$). The detailed expressions of σ_k, σ_ω, β^*, β, P_k, and P_ω can be found in (Menter, 1994; Refloch et al., 2011).

$$\frac{\partial(\rho k)}{\partial t} + \frac{\partial(\rho k\overline{u}_i)}{\partial x_i} = \frac{\partial}{\partial x_i}\left[\left(\mu + \frac{\mu_t}{\sigma_k}\right)\frac{\partial k}{\partial x_i}\right] + P_k - \beta^*\rho k\omega \quad (7)$$

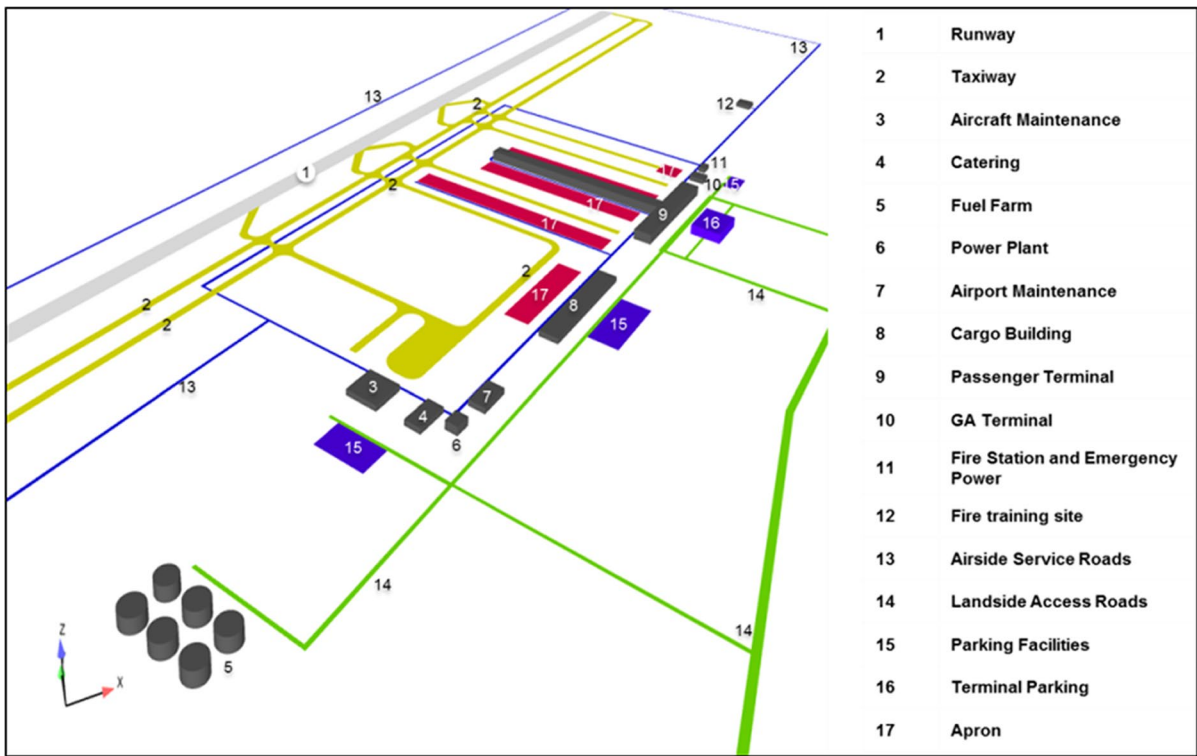|	
1	Runway
2	Taxiway
3	Aircraft Maintenance
4	Catering
5	Fuel Farm
6	Power Plant
7	Airport Maintenance
8	Cargo Building
9	Passenger Terminal
10	GA Terminal
11	Fire Station and Emergency Power
12	Fire training site
13	Airside Service Roads
14	Landside Access Roads
15	Parking Facilities
16	Terminal Parking
17	Apron

Fig. 1 CAEPport airport 3D geometry

$$\frac{\partial(\rho\omega)}{\partial t} + \frac{\partial(\rho\omega\overline{u}_i)}{\partial x_i} = \frac{\partial}{\partial x_i}\left[\left(\mu + \sigma_\omega\mu_t\right)\frac{\partial\omega}{\partial x_i}\right] + P_\omega - \beta\rho\omega^2 + D_\omega$$

$$(8)$$

3 Simulation Setup

3.1 Airport Configuration

Simulations were carried out in the CAEPport configuration as defined by the Modelling and Databases Group of The International Civil Aviation Organization (ICAO) Committee on Aviation Environmental Protection (CAEP/8). This mock airport representative of medium size airports (ICAO, 2015) was used for local air-quality (LAQ) assessment as in the modeling capabilities and inter-comparison ICAO study. In our work, the CAEPport platform was modeled in 3D (see Fig. 1) according to the two-dimensional plan provided in the database (ICAO, 2015). Table 1 gives the building heights defined in the study with the heights of the fuel farm, power plant, and terminal parking provided in ICAO (2015). The remaining

heights were specified based on typical values of real airports.

3.2 Computational Domain and Boundary Conditions

Figure 2 presents the computational domain of size 8 × 8 × 1.5 km covering the CAEPport platform, while Table 2 summarizes the boundary conditions. The airport reference point (ARP) of the CAEPport model was placed in the middle of the runway ground. The inlet and outlet surfaces are aligned with the western and eastern sides of the airport. The other

Table 1 Building heights used in the CAEPport 3D model

Building name	Building number	Height (m)
Fuel farm	5	22
Power plant	6	15
Passenger terminal	9	20
Terminal parking	16	20
Other buildings	3, 4, 7, 8, 10, 11, 12	10

two surfaces were then aligned with the northern and southern sides, so that a wind coming from the west would be normal to the inlet surface, for example.

3.3 Grid Configuration

The domain was meshed using non-structured cells composed of tetrahedral elements. Table 3 summarizes the values of the mesh size per airport part. The total number of cells was about 12.4 million. Figure 3 illustrates the surface mesh of the outer box as well as the ground in and around the CAEPport area with several close-up views.

3.4 Ambient Conditions

The mixing of air and pollutant dispersion in the atmosphere is strongly influenced by atmospheric stability. Three atmospheric stability conditions can be distinguished depending on the value of the ambient lapse rate $\left(\Gamma_{amb} = -dT/dz\right)$ as compared to the value of dry adiabatic lapse rate $\left(\Gamma_{ad} = g/c_p = 9.8\,\mathrm{K/km}\right)$. When $\left(\Gamma_{amb} = \Gamma_{ad}\right)$, the atmosphere has neutral stability. Unstable (super-adiabatic) conditions prevail when the air temperature drops more than 9.8 K/km ($\sim 1\ °\mathrm{C}/100$ m), while stable (sub-adiabatic) conditions prevail when the air temperature drops at a rate less than 9.8 K/km. The temperature inversion is a special case of sub-adiabatic conditions when the gradient of air temperature is positive and a layer of warm air exists over a layer of cold air. An unstable

Table 2 Boundary conditions

Section name	Boundary conditions
West	Inlet
East	Outlet
North	Symmetry
South	Symmetry
Ground	No-slip wall
Top	Slip wall
Airport buildings	No-slip walls

atmosphere promotes pollutant dispersion. Conversely, stable conditions result in poor pollutant dispersion, while extreme stability (inversion) traps pollutants and inhibits dispersion. Hence, the impact of atmospheric stability on NO_x emissions from the CAEPport LTO operations was investigated in the case of neutral, stable, and unstable conditions.

Ambient conditions used at the inlet boundary of the computational domain (i.e., west plane in Fig. 2) were based on both meteorological data and the chemical composition of the background atmosphere. For instance, the meteorological data provided by Météo-France (Météo-France, 2017) were based on the two experimental campaigns BLLAST (Canut et al., 2016; Lothon et al., 2014; Pietersen et al., 2015) and PASSY (Chemel et al., 2016; Paci et al., 2016) performed between 2011 and 2015. The background meteorological data shown in Fig. 4 represent

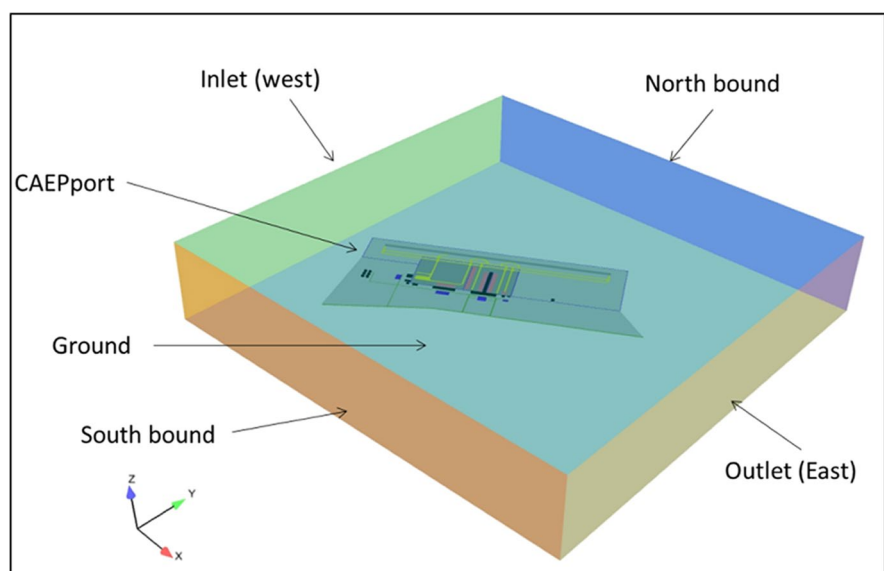**Fig. 2** Computation domain covering the CAEPport platform

Table 3 Values of mesh size by airport part

Part name	Mesh size (m)
Runway	3
Taxiway	3
Aircraft maintenance	2
Catering	2
Fuel Farm	2
Power plant	2
Airport maintenance	2
Cargo building	2
Passenger terminal	2
GA terminal	2
Fire station and emergency power	2
Fire training site	2
Airside service roads	3
Landside access roads	3
Parking facilities	5
Terminal parking	2
Apron	5
Inlet	50
Outlet	50
Lateral	50
Top	500
Ground (airport–around airport)	50

the three main scenarios selected for our study: stable (data of February 11, 2015), unstable (data of July 2, 2011), and neutral (data of June 27, 2011) atmospheres. To ensure consistency between background pollution and meteorology, ambient concentrations were modeled in 3-D at the same meteorological scenarios of latter measurement campaigns using the national prediction system of French air quality (*PREV'AIR*). Figure 5 shows the background mass fractions of both NO and NO_2 used in our study.

3.5 Aircraft Traffic and Emissions

The CAEPport database provides air-traffic information that includes a full-year journal of aircraft movements (ICAO, 2015). A specific day (i.e., October 8, 2004) was chosen since it has the maximum number of movements in the year, a total of 311 LTO movements. The peak of movements was recorded between 12:00 p.m. and 1:00 p.m. Figure 6 shows the considered LTO trajectories with the blue lines corresponding to landing and taxiing in and the red lines corresponding to taxiing out and takeoff.

Aircraft movements as well as their respective plume properties were updated every second along their trajectories (speed, position (Ghedhaifi, 2010)). For instance, each aircraft engine was considered as

Fig. 3 Mesh of the CAEPport platform and close-up views main facilities: **a** fuel farm, **b** aircraft maintenance with catering buildings, and **c** terminal
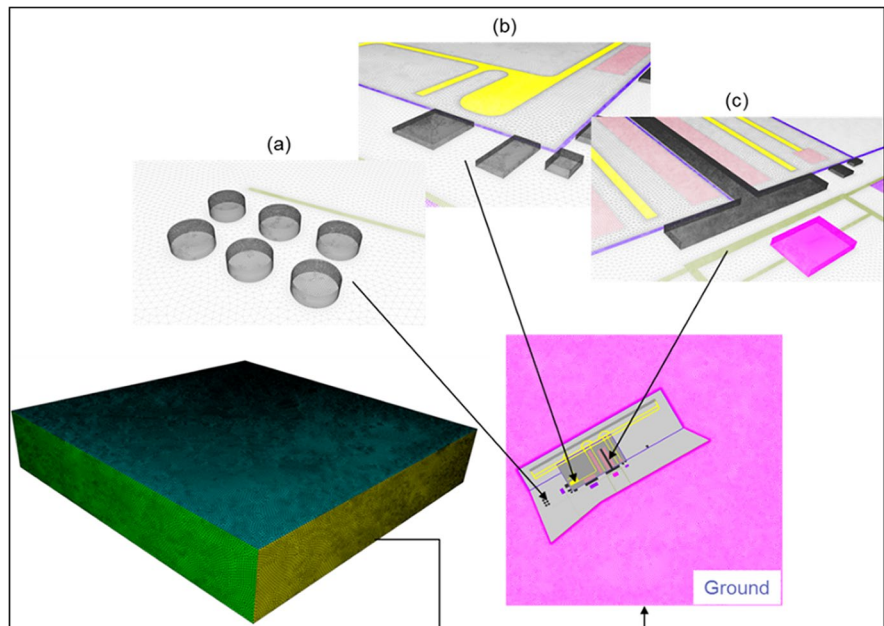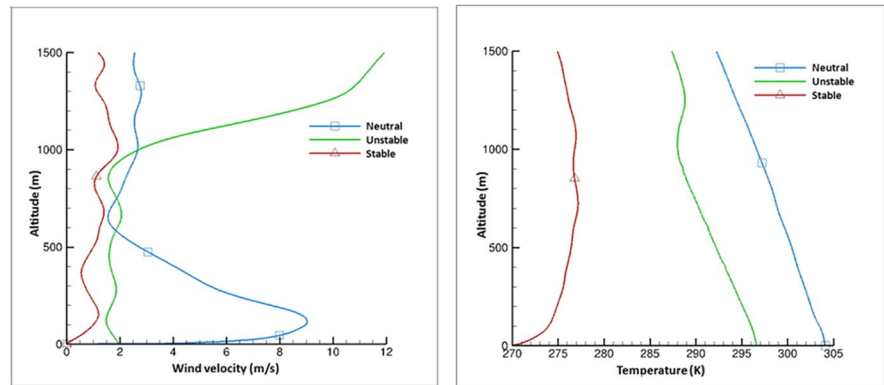
Fig. 4 Wind velocity (right) and ambient temperature (left) vs. altitude

an individual mobile source moving along its own LTO trajectory. Emission properties provided by the CAEPport database (ICAO, 2015) depend on engine type, LTO-time power settings associated with a specific exhaust temperature, speed, and chemical composition. The LTO operations also include APU emissions during parking time at aprons. One should note that many international airports offer additional equipment at terminal gates such as ground power units (GPU) and pre-conditioned air (PCA) systems that supply aircraft with electrical power and temperature-controlled cabin air, respectively, so as to reduce the APU-time usage. The latter systems are not accounted for in the present study to investigate the APU emission impact in the worst possible case scenario. Furthermore, as highlighted by Padhra (2018), the change in the use of APU due to such provision is not known other than the generally accepted notion that APU usage is likely to be reduced.

4 Results Analysis

4.1 Wind Environment

The study of the wind environment in the CAEPport platform involves the analysis of wind flow speed and pattern around its buildings. Figure 7 gives the axial mean wind velocity along a vertical plane passing through the terminal building for the three stability cases (note the different scales for the three stability cases). For instance, results clearly showed that both the stable and neutral cases preserved wind profiles imposed at the inlet boundary with mainly horizontal wind movements. This contrasts with the unstable case, in which there was an amplification of large fluctuations, suggesting both horizontal and vertical wind movements. These results helped to verify initial settings under the three atmospheric conditions studied.

The airport wind environment at the pedestrian level is also of great interest for the study of pollutant

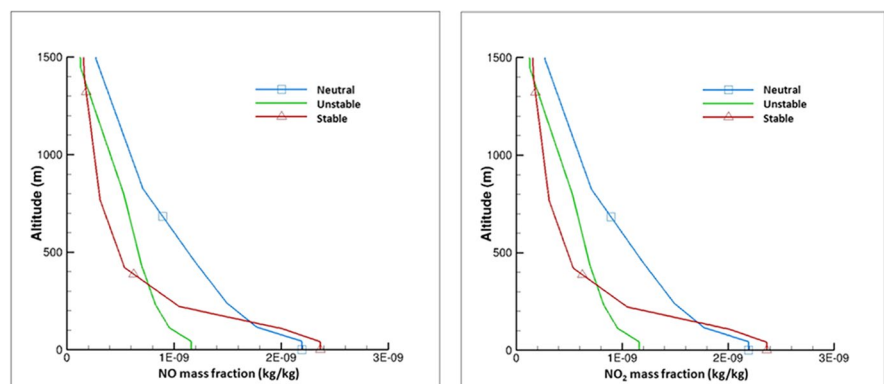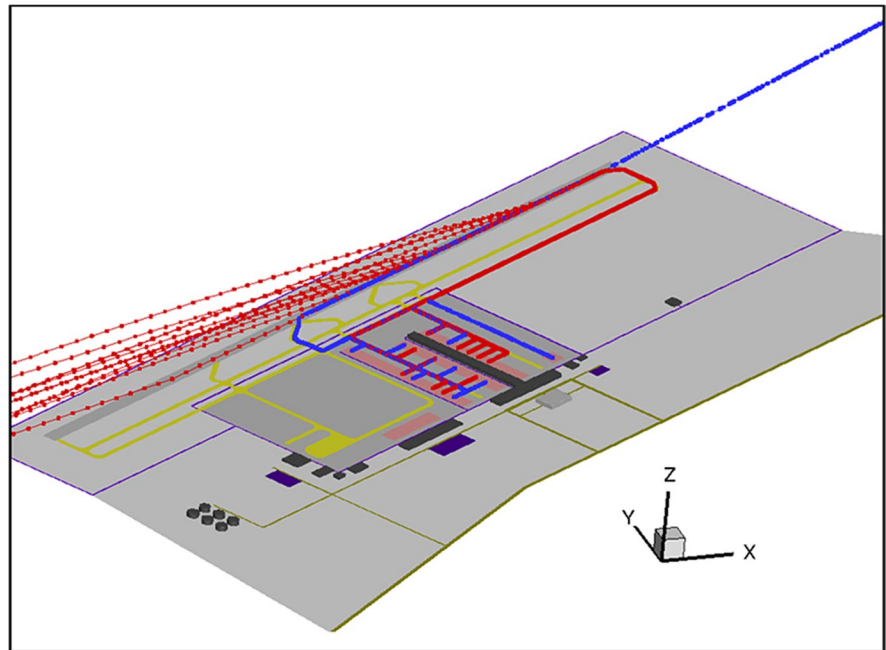**Fig. 5** Mass fractions of NO (left) and NO_2 (right) vs. altitude

Fig. 6 Simulated aircraft trajectories: landing/taxiing in (blue lines) and takeoff/taxiing out (red lines)

dispersion as it helps to locate low-velocity (i.e., low dispersion) regions. Figure 8 gives the axial mean velocity fields on a cut plane at 2 m above the ground for the three stability cases. Westerly winds (from left to right in Fig. 8) crossing the CAEPport platform create recirculation zones behind buildings (wake). The three cases show that the largest low-velocity region was located in the passenger terminal wake.

After this first verification step of flow initialization, emissions from mobile sources were implemented to investigate pollutant dispersion from airport traffic. The results are discussed in the following section.

4.2 LTO-Cycle Emissions

4.2.1 Instantaneous Distributions

Figures 9 and 10 show the results for the instantaneous pedestrian-level fields computed under stable atmospheric conditions at different times for NO and NO_2 concentrations, respectively.

At 12 p.m. (initial time), results provide background concentrations of both NO and NO_2 presented in Fig. 5. The first simulated aircraft plumes can be observed at 12:05 p.m. in Figs. 9b and 10b. The accumulation of emissions from several aircraft

plumes during LTO operations show higher concentrations of both NO and NO_2, as expected. At 12:30 p.m. (see Figs. 9c and 10 (c)), higher NO concentrations were observed in the runway threshold due to the high-power setting of main aircraft engines at takeoff. In contrast, higher NO_2 concentrations were located in the apron area due to the low power setting of main engines at taxiing in and out, along with the NO_2 contribution from APUs during extended parking. Figures 9d and 10d, corresponding to 1 p.m., illustrate the instantaneous distributions of an aircraft emission at the runway threshold but after being transported by a westerly wind.

4.2.2 Averaged Distributions

The instantaneous fields allowed for the monitoring of transient emissions during aircraft traffic, which helped to better understand differences observed at different regimes and in different LTO operation zones. Local air quality, however, has been reported on most often in the literature using averaged fields over a specified time interval to estimate chronical effects (Zimmer & Larsen, 1965) (see for example studies Henry-Lheureux et al., 2021; Koulidis et al., 2020; Popescu et al., 2011)). As such, hourly

Fig. 7 Streamwise wind velocity along a vertical plane passing through the terminal building for neutral, stable, and unstable atmospheric conditions
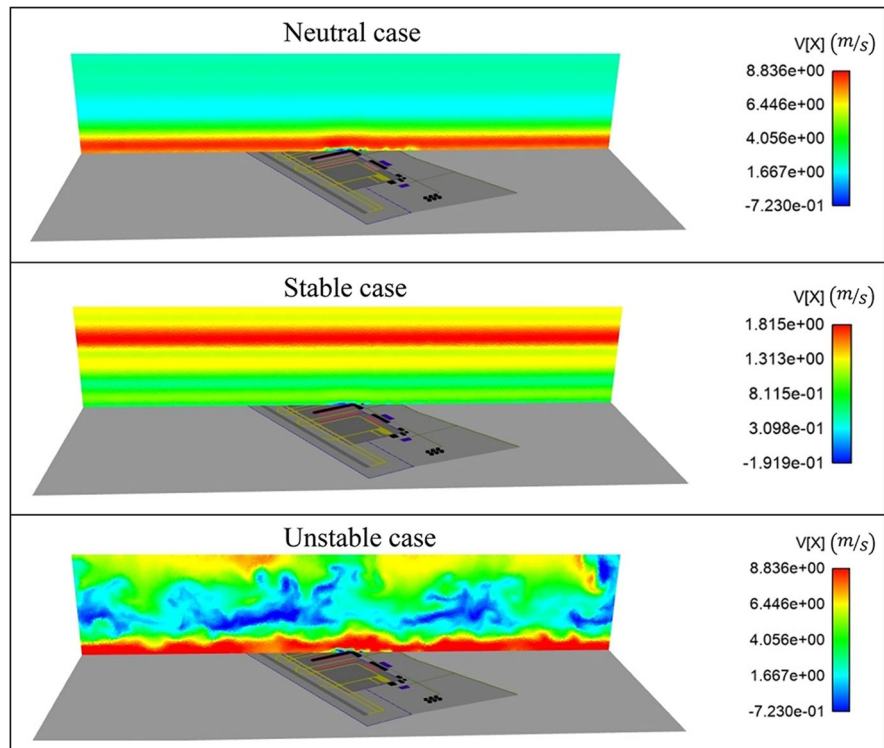
mean concentrations are presented in Fig. 11 under stable atmospheric conditions. Results of NO (left column) and NO_2 (right column) were averaged over 1 h between 12 p.m. and 1 p.m. (1st row), 1 p.m. and 2 p.m. (2nd row), and between 3 p.m. and 4 p.m. (3rd row). Averaged distributions help to locate areas where cyclic LTO emissions are recorded for 1 h. For instance, high concentrations of NO and NO_2 were observed in the apron area, on the runway threshold, and on taxiways.

The results in Fig. 11 show NO_2 emissions dominating over NO_x emissions in apron areas due to the low-power setting of main engines along with extended emissions from APUs. For instance, the APUs emitted more NO_2 than NO (Ghedhaifi, 2010). Conversely, NO emissions dominated NO_x emissions along the runway threshold mainly due to the high power setting of main aircraft engines at takeoff. The accumulation of aircraft plumes caused higher NO and NO_2 emissions (on average) between 2 p.m. and 3 p.m., as shown in Fig. 11. As such, the analysis of both atmospheric stability and APU emission impacts presented below was performed on hourly mean concentrations between 2 p.m. and 3 p.m.

4.3 Impact of Atmospheric Stability

The dispersion of aircraft NO_x emissions during LTO operations was investigated under three different atmospheric conditions corresponding to three cases of stability. Figure 12 shows the hourly mean concentration NO (left column) and NO_2 (right column) under stable (1st row), neutral (2nd row), and unstable conditions (3rd row). The results clearly show poor pollutant dispersion in the stable case (i.e., higher NO and NO_2 concentrations) than both the neutral and unstable cases. The NO_2 concentration in the three cases was relatively higher in the apron area due to the longtime parking and low power setting of aircraft engines during taxiing in and out operations. Conversely, NO_x emissions at the runway threshold were dominated by NO due to the high power setting of aircraft engines at takeoff.

4.4 Impact of APU Emissions

To assess the APU impact on airport NO_x emissions, simulations were performed with and without APUs in stable atmospheric conditions. The 1st and 2nd

Fig. 8 Axial wind velocity at the pedestrian level (2 m from the ground) for the three stability cases (top to bottom): neutral, stable, and unstable atmospheric conditions
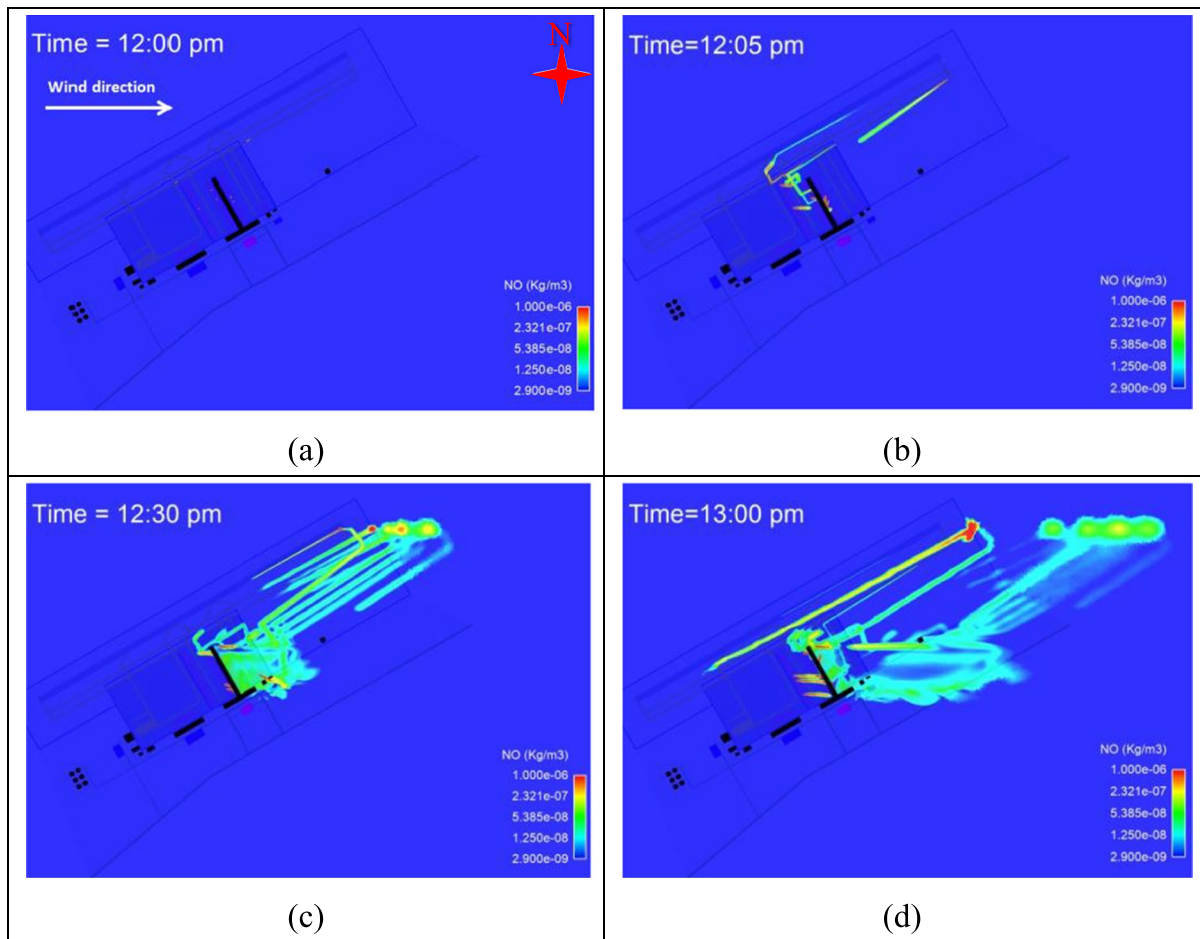

Neutral case

Stable case

Unstable case
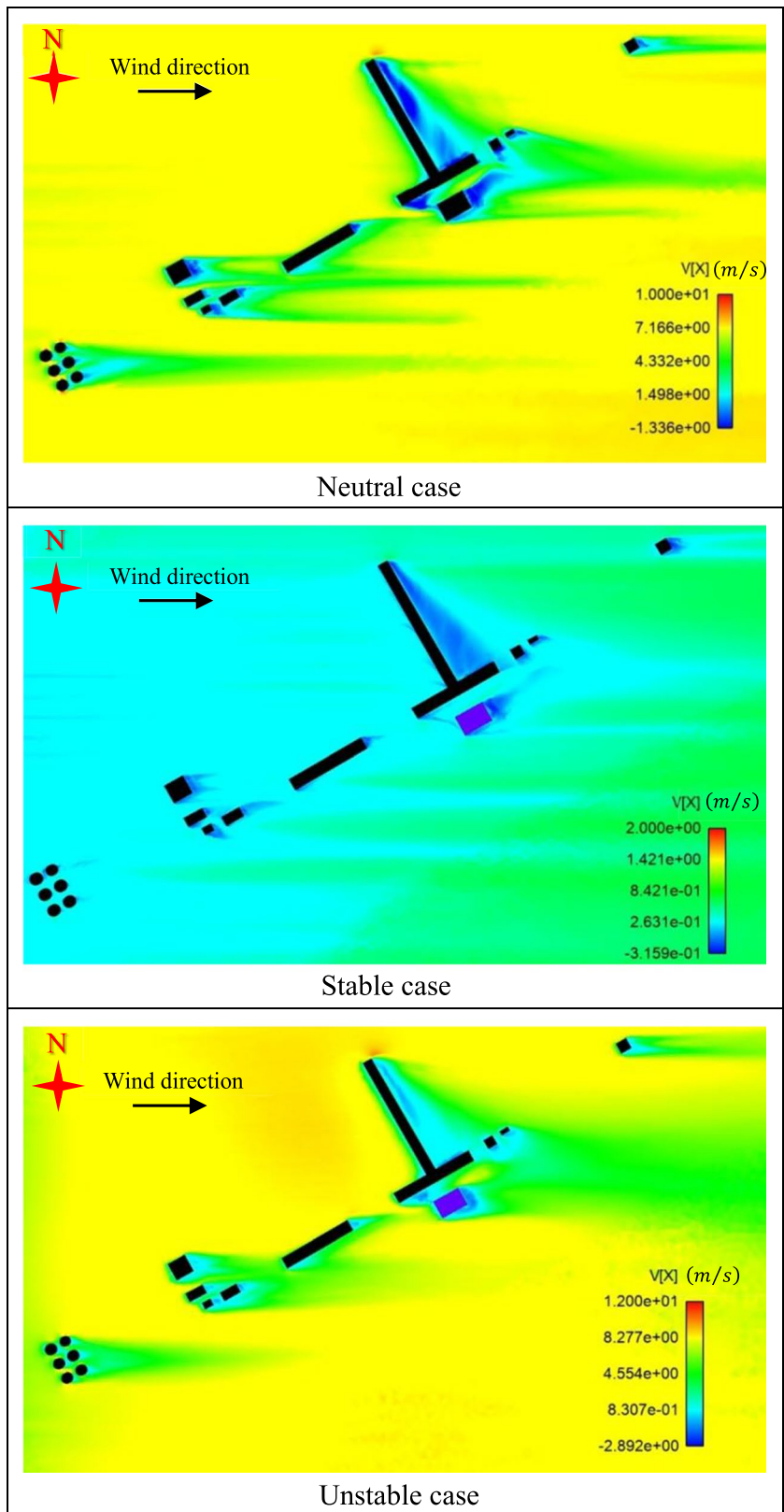
Fig. 9 Instantaneous fields of pedestrian-level NO concentration at **a** 12 p.m., **b** 12:05 p.m., **c** 12:30 pm, and **d** 1 p.m

columns, respectively, in Fig. 13 compare the NO and NO_2 concentrations.

Figure 13 (3rd row) presents the difference between concentration distributions with and without APU emissions. As illustrated, APU use caused higher NO_x concentrations around the terminal building and in its wake, as expected. A small area of NO concentration was also observed at the runway threshold due to the use of APUs during takeoff to support main engines. A comparison of NO and NO_2 emissions showed higher NO_2 concentrations than NO concentrations with APU emissions and inversely without APUs. Overall, it can be concluded that APU use contributed to higher concentrations

of NO and NO_2, and especially of NO_2 in terminal areas.

4.5 NO_2 Threshold Limit

The threshold limit of NO_2 exposure in Europe and France is 18 h of concentrations above 200 μg/m^3. Figure 14 shows the airport areas where the concentration limit (hourly average value between 2 p.m. and 3 p.m.) was above 200 μg/m3 in the three cases of atmospheric stability with APU emissions. This information could help limit risks. The results for the stable case without APUs were also compared to help understand the effect of APU emissions on local air quality.
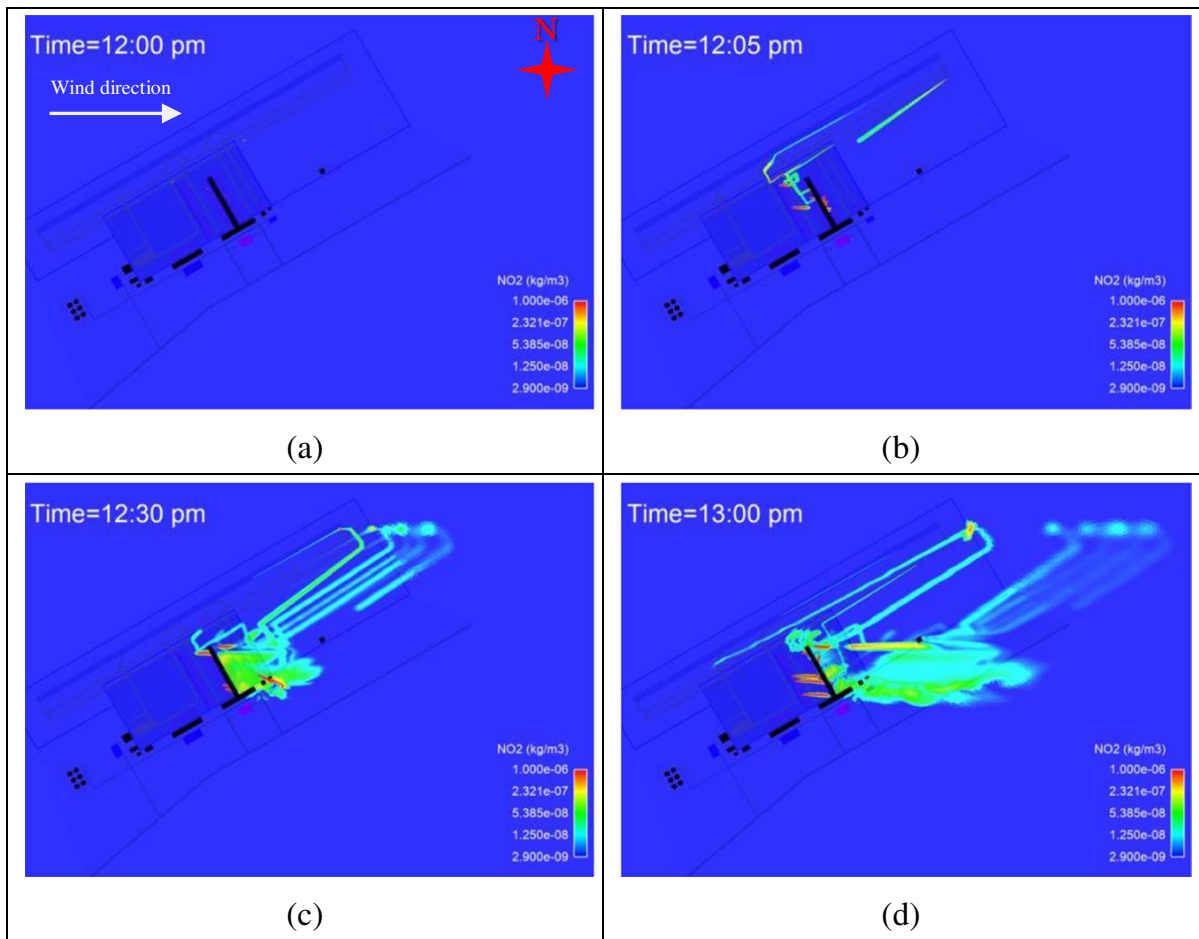
Fig. 10 Instantaneous fields of pedestrian-level NO$_2$ concentration at **a** 12 p.m., **b** 12:05 p.m., **c** 12:30 p.m., and **d** 1 p.m

For the neutral and unstable conditions presented in the 1st and 2nd rows in Fig. 14, respectively; no area above the threshold limit was detected between 2 p.m. and 3 p.m. In contrast, stable atmospheric conditions (Fig. 14, 3rd row) caused an accumulation of pollutant emissions in the terminal area and its wake. The results without APUs under the same conditions (Fig. 14, 4th row) show that the NO$_2$ accumulation was primarily due to APU use on aprons. Thus, the impact of NO$_2$ emissions could be considerably reduced without APUs. As such, only a very small area was detected above the threshold limit with high power settings on the threshold runway.

5 Conclusion

High-resolution CFD simulations of NO$_x$ emission dispersion were carried out with the CAEPport configuration. The 3D modeling accounts for both aircraft engines and APU-related emissions during the LTO cycle and parking time, respectively. NO$_x$ dispersion results helped to better investigate differences observed during successive LTO cycles. For instance, higher NO concentrations were observed on the runway threshold, while higher NO$_2$ concentrations were observed in the apron area due to (1) the different power settings for main aircraft engines at takeoff and taxiing in and out and (2) to the APU contribution
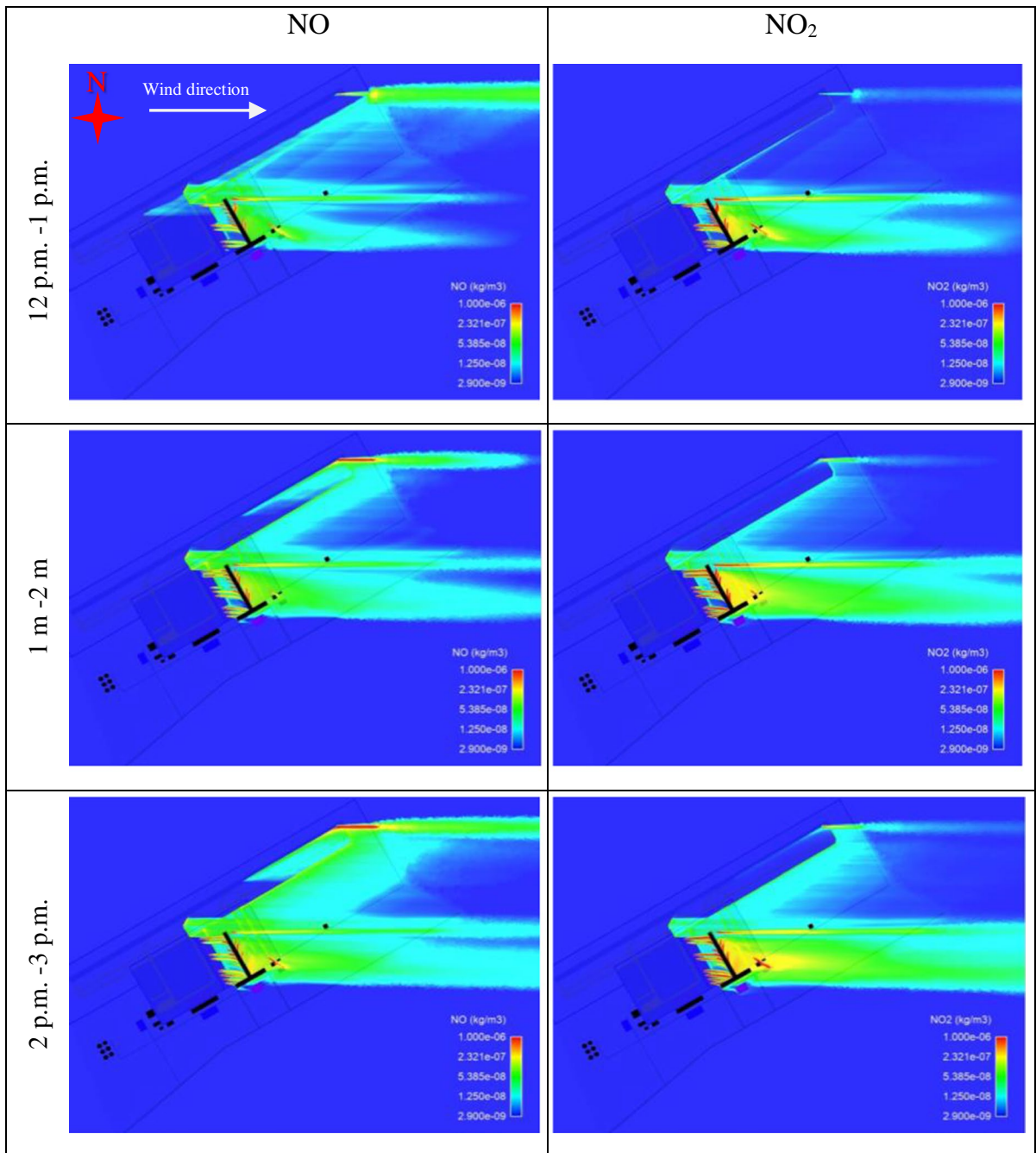
Fig. 11 Hourly mean concentrations of NO (left column) and NO$_2$ (right column), between 12 p.m. and 1 p.m. (1st row), 1 p.m. and 2 p.m. (2nd row), and 2 p.m. and 3 p.m. (3rd row)
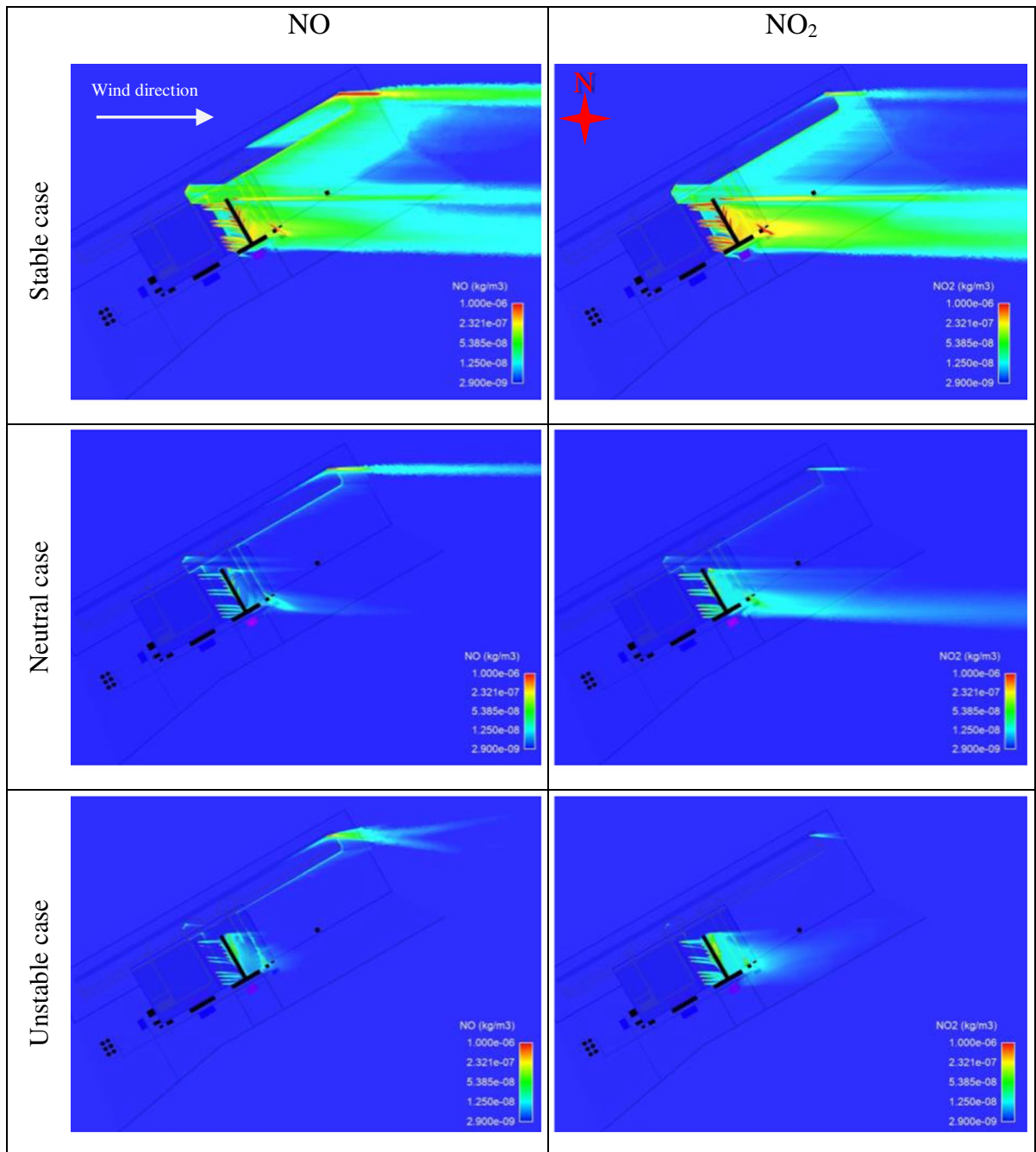
Fig. 12 Hourly mean concentrations of NO (left column) and NO$_2$ (right column) for three atmospheric cases: stable (1st row), neutral (2nd row), and unstable (3rd row)
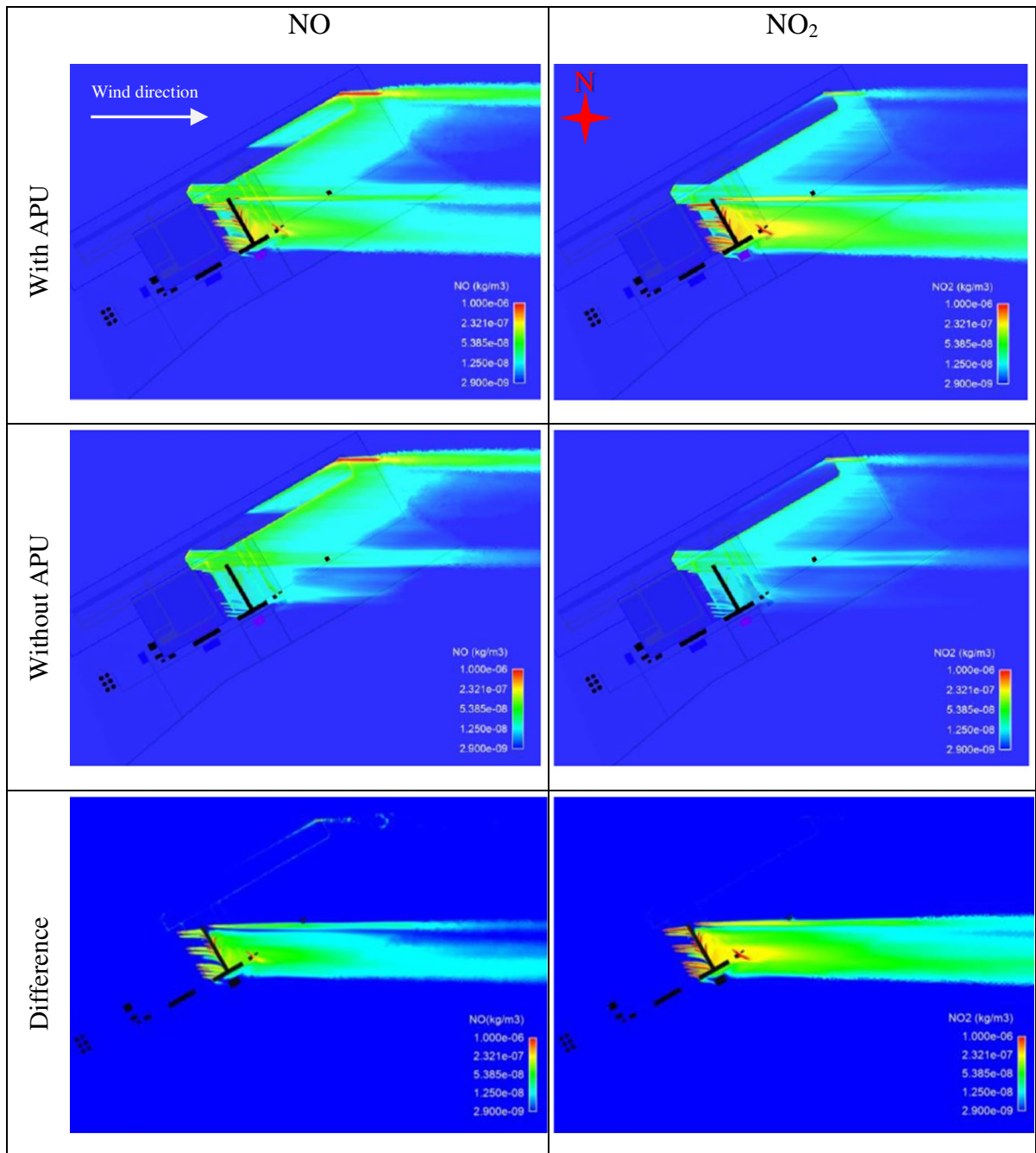
Fig. 13 Hourly mean concentration of NO (left column) and NO$_2$ (right column) with APU emissions (1st row), without APU emissions (2nd row), and the difference between the two cases (3rd row)

during extended parking. The accumulation of air-craft plumes during LTO operations caused higher NO and NO$_2$ emissions. Further analysis of averaged distributions confirmed the domination of NO$_2$ on

NO$_x$ emissions in apron areas, with NO dominating in the runway threshold area. Stable atmospheric conditions show poorer pollutant dispersion compared to both the neutral and unstable cases. As for the APU
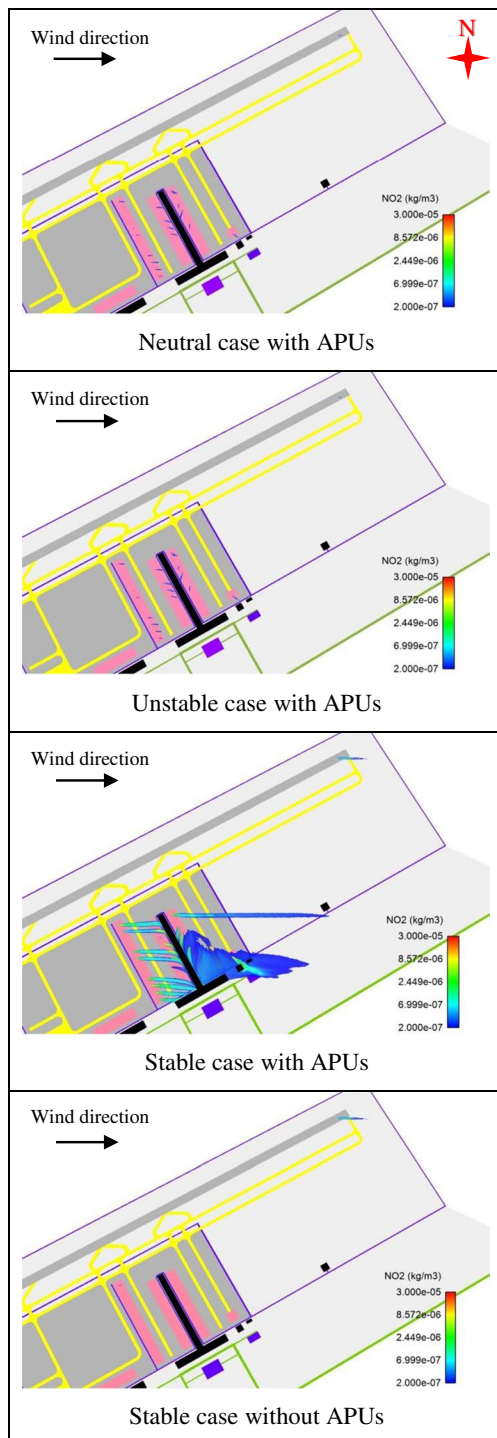
Fig. 14 Hourly average concentrations of NO_2 above 200 μg/m.^{3}

emission impact, there are higher concentrations of both NO and NO_2 emissions and especially of NO_2 in terminal areas. As a recommendation, electric devices can be used on aprons instead of traditional APUs to reduce the impact of NO_2 emissions around the terminal.

The proposed model helped to better represent the microscale evolution of aircraft emissions, both spatially and temporally, and persistently high concentration spots were identified with high fidelity. The model can hence serve as a decision-making tool for airport air-quality assessments or to investigate the impact of different operational strategies as potential mitigation solutions. Future simulations should account for species reactivity and ground radiative properties (tar, vegetation, etc.). Volatile and ultrafine particles (with diameters of less than 100 nm) are of great interest due to their toxicity and thus need to be investigated in future works.

Data availability Not applicable.

Declarations

Conflict of Interest The authors declare no competing interests.

References

Canut, G., Couvreux, F., Lothon, M., Legain, D., Piguet, B., Lampert, A., Maurel, W., & Moulin, E. (2016). Turbulence fluxes and variances measured with a sonic anemometer mounted on a tethered balloon. *Atmospheric Measurement Techniques, 9*(9), 4375–4386. https://doi.org/10.5194/amt-9-4375-2016

Celikel, A., Duchene, N., Fuller, I., Silue, M., Fleuti, E., Hofmann, P., & Moore, T. (2004). *Airport local air quality studies; case study: emission inventory for Zurich Airport with different methodologies*. Reference number: EEC/SEE/2004/010. European Organisation for the Safety of Air Navigation EUROCONTROL July 2004. https://www.eurocontrol.int/sites/default/files/library/034_ALAQS_Emission_Inventory_for_Zurich_Airport.pdf. Accessed 15 Aug 2021

Chemel, C., Arduini, G., Staquet, C., Largeron, Y., Legain, D., Tzanos, D., & Paci, A. (2016). Valley heat deficit as a bulk measure of wintertime particulate air pollution in

the Arve River Valley. *Atmospheric Environment, 128*, 208–215. https://doi.org/10.1016/j.atmosenv.2015.12.058

Chester, M. V., & Horvath, A. (2009). Environmental assessment of passenger transportation should include infrastructure and supply chains. *Environmental Research Letters, 4*(2), 024008. https://doi.org/10.1088/1748-9326/4/2/024008

Crecelius, H., & Sommerfeld, M. (2005). Air quality monitoring of Frankfurt Airport. *GEFAHRSTOFFE REINHALTUNG DER LUFT, 65*(1–2), 49–54.

Du, Y., Blocken, B., & Pirker, S. (2020). A novel approach to simulate pollutant dispersion in the built environment: transport-based recurrence CFD. *Building and Environment, 170*, 106604. https://doi.org/10.1016/j.buildenv.2019.106604

Farias, F., & ApSimon, H. (2006). Relative contributions from traffic and aircraft NO_x emissions to exposure in West London. *Environmental Modelling & Software, 21*(4), 477–485. https://doi.org/10.1016/j.envsoft.2004.07.010

Ghedhaifi, W. (2010). *Chemical impact of aviation in airport areas* 27th Congress of International Council of the Aeronautical Sciences (ICAS), Nice, France. http://www.icas.org/ICAS_ARCHIVE/ICAS2010/PAPERS/737.PDF. Accessed 15 Aug 2021

Gudmundsson, S. V., Cattaneo, M., & Redondi, R. (2021). Forecasting temporal world recovery in air transport markets in the presence of large economic shocks: the case of COVID-19. *Journal of Air Transport Management, 91*, 102007. https://doi.org/10.1016/j.jairtraman.2020.102007

Hanna, S. R., Brown, M. J., Camelli, F. E., Chan, S. T., Coirier, W. J., Hansen, O. R., Huber, A. H., Kim, S., & Reynolds, R. M. (2006). Detailed simulations of atmospheric flow and dispersion in downtown Manhattan: An application of five computational fluid dynamics models. *Bulletin of the American Meteorological Society, 87*(12), 1713–1726. https://doi.org/10.1175/BAMS-87-12-1713

Henry-Lheureux, T., Seers, P., Ghedhaïfi, W., & Garnier, F. (2021). Overview of emissions at Montreal's Pierre Elliott Trudeau International airport and impact of local weather on related pollutant concentrations. *Water, Air, & Soil Pollution, 232*(5), 173. https://doi.org/10.1007/s11270-021-05087-2

ICAO. (2015). *Assembly of the CAEPport Database* (Modeling and Databases Group of the Committee on Aviation Environmental Protection (CAEP), Issue.

ICAO. (2021). *Post-Covid-19 forecasts scenarios.* Traffic forecasts scenarios (EB.21.28). https://www.icao.int/sustainability/Documents/Post-COVID-19%20forecasts%20scenarios%20tables.pdf. Accessed 15 Aug 2021

Kinsey, J. S., Timko, M. T., Herndon, S. C., Wood, E. C., Yu, Z., Miake-Lye, R. C., Lobo, P., Whitefield, P., Hagen, D., Wey, C., Anderson, B. E., Beyersdorf, A. J., Hudgins, C. H., Thornhill, K. L., Winstead, E., Howard, R., Bulzan, D. I., Tacina, K. B., & Knighton, W. B. (2012). Determination of the emissions from an aircraft auxiliary power unit (APU) during the Alternative Aviation Fuel Experiment (AAFEX). *Journal of the Air & Waste Management Association, 62*(4), 420–430. https://doi.org/10.1080/10473289.2012.655884

Koulidis, A. G., Progiou, A. G., & Ziomas, I. C. (2020). Air quality levels in the vicinity of three major Greek airports.

Environmental Modeling & Assessment, 25(6), 749–760. https://doi.org/10.1007/s10666-020-09699-6

Lothon, M., Lohou, F., Pino, D., Couvreux, F., Pardyjak, E. R., Reuder, J., Vilà-Guerau de Arellano, J., Durand, P., Hartogensis, O., Legain, D., Augustin, P., Gioli, B., Lenschow, D. H., Faloona, I., Yagüe, C., Alexander, D. C., Angevine, W. M., Bargain, E., Barrié, J., … Zaldei, A. (2014). The BLLAST field experiment: Boundary-layer late afternoon and sunset turbulence. *Atmospheric Chemistry and Physics, 14*(20), 10931–10960. https://doi.org/10.5194/acp-14-10931-2014

Masiol, M., & Harrison, R. M. (2014). Aircraft engine exhaust emissions and other airport-related contributions to ambient air pollution: a review. *Atmospheric Environment, 95*, 409–455. https://doi.org/10.1016/j.atmosenv.2014.05.070

Mazaheri, M., Johnson, G. R., & Morawska, L. (2011). An inventory of particle and gaseous emissions from large aircraft thrust engine operations at an airport. *Atmospheric Environment, 45*(20), 3500–3507. https://doi.org/10.1016/j.atmosenv.2010.12.012

Mei, S.-J., Luo, Z., Zhao, F.-Y., & Wang, H.-Q. (2019). Street canyon ventilation and airborne pollutant dispersion: 2-D versus 3-D CFD simulations. *Sustainable Cities and Society, 50*, 101700. https://doi.org/10.1016/j.scs.2019.101700

Menter, F. R. (1994). Two-equation eddy-viscosity turbulence models for engineering applications. *AIAA Journal, 32*(8), 1598–1605. https://doi.org/10.2514/3.12149

Météo-France. (2017). *Research report 2017* (ISSN: 2116–438X). C. N. d. R. M.-U. 3589. https://www.umr-cnrm.fr/IMG/pdf/rr_2017_fr_web.pdf. Accessed 15 Aug 2021

Nižetić, S. (2020). Impact of coronavirus (COVID-19) pandemic on air transport mobility, energy, and environment: a case study. *International Journal of Energy Research, 44*(13), 10953–10961. https://doi.org/10.1002/er.5706

Paci, A., Staquet, C., Allard, J., Barral, H., Canut, G., Cohard, J., Jaffrezo, J., Martinet, P., Sabatier, T., & Troude, F. (2016). The Passy-2015 field experiment: atmospheric dynamics and air quality in the Arve River Valley. *Pollution Atmosphérique, 271*(10.4267).

Padhra, A. (2018). Emissions from auxiliary power units and ground power units during intraday aircraft turnarounds at European airports. *Transportation Research Part D: Transport and Environment, 63*, 433–444. https://doi.org/10.1016/j.trd.2018.06.015

Pietersen, H. P., Vilà-Guerau de Arellano, J., Augustin, P., van de Boer, A., de Coster, O., Delbarre, H., Durand, P., Fourmentin, M., Gioli, B., Hartogensis, O., Lohou, F., Lothon, M., Ouwersloot, H. G., Pino, D., & Reuder, J. (2015). Study of a prototypical convective boundary layer observed during BLLAST: Contributions by large-scale forcings. *Atmospheric Chemistry and Physics, 15*(8), 4241–4257. https://doi.org/10.5194/acp-15-4241-2015

Pontiggia, M., Derudi, M., Alba, M., Scaioni, M., & Rota, R. (2010). Hazardous gas releases in urban areas: assessment of consequences through CFD modelling. *Journal of Hazardous Materials, 176*(1), 589–596. https://doi.org/10.1016/j.jhazmat.2009.11.070

Popescu, F., Ionel, I., & Talianu, C. (2011). Evaluation of air quality in airport areas by numerical simulation. *Environmental Engineering & Management Journal (EEMJ), 10*(1), 115–120. https://doi.org/10.30638/eemj.2011.016

Refloch, A., Courbet, B., Murrone, A., Villedieu, P., Laurent, C., Gilbank, P., Troyes, J., Tessé, L., Chaineray, G., Dargaud, J. B., Quémerais, E., & Vuillot, F. (2011). *CEDRE Software*. In *AerospaceLab*. https://hal.archives-ouvertes.fr/hal-01182463. Accessed 15 Aug 2021

Santos, J. M., Reis, N. C., Goulart, E. V., & Mavroidis, I. (2009). Numerical simulation of flow and dispersion around an isolated cubical building: the effect of the atmospheric stratification. *Atmospheric Environment, 43*(34), 5484–5492. https://doi.org/10.1016/j.atmosenv.2009.07.020

Sarrat, C., Aubry, S., Chaboud, T., & Lac, C. (2017). Modelling airport pollutants dispersion at high resolution. *Aerospace, 4*(3), 46. https://www.mdpi.com/2226-4310/4/3/46. Accessed 15 2021

Suppan, P., & Graf, J. (2000). The impact of an airport on regional air quality at Munich, Germany. *International Journal of Environment and Pollution, 14*(1–6), 375–381.

Targino, A. C., Machado, B. L. F., & Krecl, P. (2017). Concentrations and personal exposure to black carbon particles at airports and on commercial flights. *Transportation Research Part D: Transport and Environment, 52*, 128–138. https://doi.org/10.1016/j.trd.2017.03.003

Tominaga, Y., & Stathopoulos, T. (2009). Numerical simulation of dispersion around an isolated cubic building: comparison of various types of k-ε models. *Atmospheric Environment, 43*(20), 3200–3210. https://doi.org/10.1016/j.atmosenv.2009.03.038

Tominaga, Y., & Stathopoulos, T. (2013). CFD simulation of near-field pollutant dispersion in the urban environment: a review of current modeling techniques. *Atmospheric Environment, 79*, 716–730. https://doi.org/10.1016/j.atmosenv.2013.07.028

Tominaga, Y., & Stathopoulos, T. (2016). Ten questions concerning modeling of near-field pollutant dispersion in the built environment. *Building and Environment, 105*, 390–402. https://doi.org/10.1016/j.buildenv.2016.06.027

Winther, M., Kousgaard, U., Ellermann, T., Massling, A., Nøjgaard, J. K., & Ketzel, M. (2015). Emissions of NO$_x$, particle mass and particle numbers from aircraft main engines, APU's and handling equipment at Copenhagen Airport. *Atmospheric Environment, 100*, 218–229. https://doi.org/10.1016/j.atmosenv.2014.10.045

Yang, X., Cheng, S., Wang, G., Xu, R., Wang, X., Zhang, H., & Chen, G. (2018). Characterization of volatile organic compounds and the impacts on the regional ozone at an international airport. *Environmental Pollution, 238*, 491–499. https://doi.org/10.1016/j.envpol.2018.03.073

Yim, S. H. L., Stettler, M. E. J., & Barrett, S. R. H. (2013). Air quality and public health impacts of UK airports. Part II: impacts and policy assessment. *Atmospheric Environment, 67*, 184–192. https://doi.org/10.1016/j.atmosenv.2012.10.017

Yim, S. H. L., Lee, G. L., Lee, I. H., Allroggen, F., Ashok, A., Caiazzo, F., Eastham, S. D., Malina, R., & Barrett, S. R. H. (2015). Global, regional and local health impacts of civil aviation emissions. *Environmental Research Letters, 10*(3), 034001. https://doi.org/10.1088/1748-9326/10/3/034001

Yu, H., & Thé, J. (2016). Validation and optimization of SST k-ω turbulence model for pollutant dispersion within a building array. *Atmospheric Environment, 145*, 225–238. https://doi.org/10.1016/j.atmosenv.2016.09.043

Zhang, Y., Yang, X., Yang, H., Zhang, K., Wang, X., Luo, Z., Hang, J., & Zhou, S. (2020). Numerical investigations of reactive pollutant dispersion and personal exposure in 3D urban-like models. *Building and Environment, 169*, 106569. https://doi.org/10.1016/j.buildenv.2019.106569

Zimmer, C. E., & Larsen, R. I. (1965). Calculating air quality and its control. *Journal of the Air Pollution Control Association, 15*(12), 565–572. https://doi.org/10.1080/00022470.1965.10468424